A Multiscale Evaluation of Polymer Injectivity and Fracture Behavior in the Wara Reservoir in the Burgan Field

Mohammad B. AlAbdullah[1]*, Meshal Algharaib[1], Randall S. Seright[2], and Abbas Sanaseeri[3]

[1]Kuwait University, Kuwait
[2]New Mexico Institute of Mining & Technology, Socorro, NM, USA
[3]Kuwait Oil Company, Ahmadi, Kuwait

Summary

This paper provides a comprehensive analysis of polymer injectivity in the Wara reservoir in the Burgan field in Kuwait. Polymer flooding in the Wara reservoir is a strategic objective for the field plan to reach the Kuwait oil production target. The study presents and analyzes corefloods, rheological polymer measurements, fracture pressure field measurements, and long-term polymer field injectivity tests. All the data have been critically evaluated using analytical models to assess the polymer injectivity and potential fracture initiation and extension.

Laboratory measurements of polymer bulk and in-situ viscosity were conducted using viscometers, while corefloods assessed the viscoelasticity of hydrolyzed polyacrylamide (HPAM) polymers under reservoir conditions [55°C, 162,000 ppm total dissolved solids (TDS)]. Step-rate tests in the field determined fracture initiation pressures, and long-term injectivity tests were performed at multiple rates. Field pressure responses were analyzed alongside coreflood results using the unified viscoelastic injectivity model (UVIM) coupled with a Perkins-Kern-Nordgren (PKN) fracture model. Geomechanical studies provided insights into fracture direction. This integrated approach ensured a thorough understanding of fracture initiation and polymer behavior.

Initial predictions suggested that no fractures would occur during polymer injection. However, detailed analyses revealed that (assuming that severe mechanical degradation of the polymer did not occur) fractures were indeed present. This conclusion was drawn by comparing the polymer injectivity at various polymer concentrations with that of water injectivity. Polymer injectivity was found to be independent of polymer concentration, indicating potential in-situ fracture formation/extension due to polymer viscoelasticity. Laboratory coreflood experiments confirmed these findings, demonstrating that when the injection velocity exceeds 6–10 ft/day, the polymer's extensional viscosity increases due to viscoelastic effects. As a result, the calculated pressure increases toward surpassing the fracture pressure of 2,500 psi (as measured in step-rate tests). The UVIM fracture model estimated a fracture extension of approximately 90 ft from the well. These findings are crucial for the effective planning of field-scale polymer flooding. The analysis indicates a need to clearly define the objective and design of polymer flooding within the high-permeability contrast Wara formation.

This study provides critical insights into polymer injectivity and fracture management in the world's largest sandstone oil field. It offers a novel, data-driven workflow for optimizing polymer flooding, addressing fracture risks from laboratory to field scale. The results suggest a correlation between rheo-thickening at elevated velocities and the onset of polymer-induced fracture behavior, offering a basis for improved understanding and potential optimization of polymer flooding practices.

Introduction

Polymer Viscoelasticity and Injectivity Literature. Polymer flooding is considered one of the most successful chemical-enhanced oil recovery methods, aiming to increase aqueous phase viscosity to improve oil sweep efficiency. Synthetic polymers (e.g., HPAM) are commonly used for field implementation due to their availability and low cost. Their non-Newtonian and viscoelastic rheological behavior makes predicting their in-situ injectivity a nontrivial problem in the field (Seright et al. 2009).

In viscometers and in porous media at low velocities, HPAM polymers exhibit shear-thinning behavior, where viscosity decreases as shear rates increase. However, at higher velocities in porous media, the viscoelastic properties of HPAMs make the apparent viscosity increase with increased velocity. These properties become more pronounced with higher molecular weights and polymer concentrations (Qi et al. 2017; Erincik et al. 2018). Viscoelasticity is a time-dependent phenomenon involving the relaxation and contraction of polymer chains during flow. Multiple interpretations have been offered to describe and explain the phenomenon (Dupas et al. 2013; Seright et al. 2025). Most recently, Seright et al. (2025) provided evidence to support a mechanism proposed by Chauveteau (1981) and Southwick and Manke (1988). Specifically, if the polymer relaxation time exceeds the residence time, the polymer molecules expend energy to elongate (Seright et al. 2025), resulting in shear-thickening and increased apparent viscosity (extensional viscosity). Residence time (in a pore) is inversely proportional to fluid velocity (Azad 2023).

Although the use of the terms "shear-thickening" and "shear-thinning" may seem inappropriate to some purists (because of the complicated flow field within porous media), we consistently use these terms throughout the paper simply because they are commonly used within the SPE literature. Alternatives such as "dilatant," "pseudodilatant," "rheo-thickening," "extensional-thickening," "flow-thickening," "porous-media-thickening," "elastic turbulence," and "viscoelastic" have been proposed as more appropriate (Seright et al. 2023). Still, there is no common agreement at present. We recognize that the "thickening" is entirely due to elongation of polymer passing through pore constrictions (Seright et al. 2025)—and has little or nothing to do with a pure shear field. Nevertheless, because of common usage (and rare usage of the other terms listed above), we use the terms "shear thickening" and "shear thinning" here and apologize for the misleading implications of the terms.

*Corresponding author; email: Mohammad.Abdullah1@ku.edu.kw

This paper (SPE 224998) was accepted for presentation at the SPE Conference at Oman Petroleum & Energy Show, Muscat, Oman, 12–14 May 2025, and revised for publication. Original manuscript received for review 28 June 2025. Revised manuscript received for review 6 January 2026. Paper peer approved 12 January 2026.

Shear-thickening or elongational viscoelastic behavior occurs at high rates. It becomes especially critical near unfractured injection wells, where fluid velocities are highest (Seright 1983; Delshad et al. 2008; Glasbergen et al. 2015; Seright et al. 2023). Such behavior can significantly decrease injectivity as the aqueous phase viscosity increases (Wang et al. 2008; Seright et al. 2009). However, field studies often reported unexpectedly high injectivity under such conditions. This improvement is attributed to the extension of fractures around the wellbore, induced by elevated injection pressures that exceed the reservoir's parting pressure (Clemens et al. 2013; Manichand et al. 2013; Zechner et al. 2015; Melo et al. 2017; Seright 2017; Dandekar et al. 2021).

Sagyndikov et al. (2022) reviewed over 43 years of polymer flooding field trials, finding that elongational viscosity near the injector causes fractures in all vertical injection wells. The orientation and extent of these fractures are critical for polymer sweep efficiency. If fractures extend more than one-third of the interwell distance and align toward the producer, the sweep efficiency can be significantly compromised (Dyes et al. 1958; Lee et al. 2011; Seright 2017).

In this study, polymer injectivity and fracture extension in the Wara formation of the Greater Burgan field are systematically examined (assuming that severe mechanical degradation of the polymer did not occur). The analysis combines laboratory-scale studies of polymer bulk and in-situ rheology, analytical models based on the Darcy equation, and a viscoelastic injectivity model (Abdullah et al. 2023a, 2023b), and field injectivity tests integrated with geomechanical properties. These approaches aim to predict polymer-induced fracture initiation and growth while evaluating fracture extension and direction in the Wara formation. Additional supporting figures can be found in **Appendix A**.

Reservoir Background. The Wara formation is part of the Greater Burgan field in Kuwait, the world's second-largest field. The field's oil production began in 1946, characterized by high productivity due to the exceptional Darcy permeability of the Burgan and Wara formations. The field's daily production is approximately 70% of Kuwait's daily oil production. The Wara formation is a significant contributor to the field's production (Al-Murayri et al. 2022). The Wara formation consists of multiple sandstone layers, with a gross thickness ranging from 140 ft to 180 ft and exhibiting both vertical and horizontal lithological variations. In 2014, water injection started for pressure maintenance. Feasibility studies have demonstrated Wara's significant potential for chemical enhanced oil recovery, specifically highlighting polymer flooding as an extension to waterflooding for field-scale implementation (Al-Murayri et al. 2021). Three long injectivity tests were conducted with water and polymer injected in the Wara formation. The tests aimed to assess polymer injectivity and maximum allowable injection rate and pressure for further field implementation (Al-Murayri et al. 2022; Al-Qattan et al. 2024). Through this study, the focus will be on the field tests on Well-A.

General Characteristics of the Wara Formation (Al-Murayri et al. 2021; Al-Qattan et al. 2024; Filak et al. 2017):

- Depth (ft): 4,000 (datum)
- Porosity: 0.10–0.25
- Horizontal permeability (md): 1–5,000 md
- Initial pressure (psi): 2,100 (@datum)
- Current pressure (psi): 1,600 (@datum)
- Temperature (°C): 55 (@datum)
- Connate water salinity (ppm TDS): 160,000
- Wettability: Water wet
- Oil viscosity at reservoir temperature (cp): 3
- Stock-tank oil API gravity: 27–30

Methodology

Experimental Work. To evaluate polymer injectivity, we investigated the rheological properties of polymer solutions in a viscometer and in-situ porous media. We used the same polymer conditions as those in the field injectivity test. ZLPAM-40520 (a ZL Chemicals product—commercial grade) polymer was used with a molecular weight ranging from 5 to 10 million Daltons and contains 15–20% ATBS (Al-Murayri et al. 2022). The brine used in the experiments was a synthetic composition based on field-available brine, as detailed in **Table 1**. A polymer solution with a concentration of 1,800 ppm was prepared, and its viscosity (vs. shear rate) was measured at temperatures of 25°C and 55°C using an ARES G2 viscometer **(Fig. 1)**. Single-phase coreflood experiments were conducted by sequentially injecting water and polymer solution **(Table 2)**. The maximum fluid (Darcy) velocity tested was 200 ft/day, approximating the calculated Darcy velocity at the perforation on the zone of interest of Well-A. Water injection commenced at the lowest Darcy velocity of 1 ft/day. It was gradually increased to the maximum velocity of 200 ft/day to determine the permeability and assess the occurrence of the inertia effects at the highest rates. Subsequently, polymer injection was initiated at the highest rates and then gradually decreased to the lowest rates. Although the reservoir temperature is 55°C, temperature logs indicated a cooling effect from historical water injection to approximately 30°C. Therefore, as the primary focus of this paper is to examine fracture extension caused by polymer viscoelasticity near the wellbore, we considered room temperature to be an acceptable approximation of the near-wellbore temperature. However, Seright et al. (2023) conducted coreflood experiments in Berea sandstone to evaluate the influence of temperature on polymer rheology, using 0.2% HPAM dissolved in 0.105% TDS brine. The study revealed that the resistance factor response to temperature did not follow the classical Arrhenius behavior; instead, polymer resistance factor increased more significantly than predicted. A key observation was the shift in the onset velocity of shear thickening (uonset = umin). Between 20°C and 60°C, this onset velocity increased by approximately 1.5 times for every 20°C rise in temperature. In contrast, water viscosity decreased over the same temperature interval by about the same factor of 1.5, highlighting the strong temperature sensitivity of the polymer system compared with the base fluid. **Fig. 2** illustrates the experimental setup; three accumulators per fluid are connected to achieve the high injection velocities required.

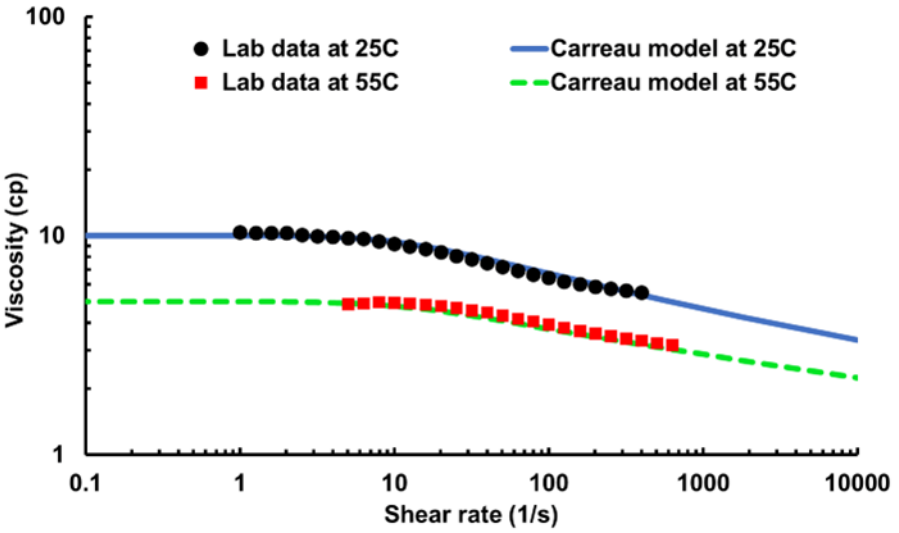

Fig. 1—ZLPAM-40520 bulk viscosity measured at 25°C and 55°C.

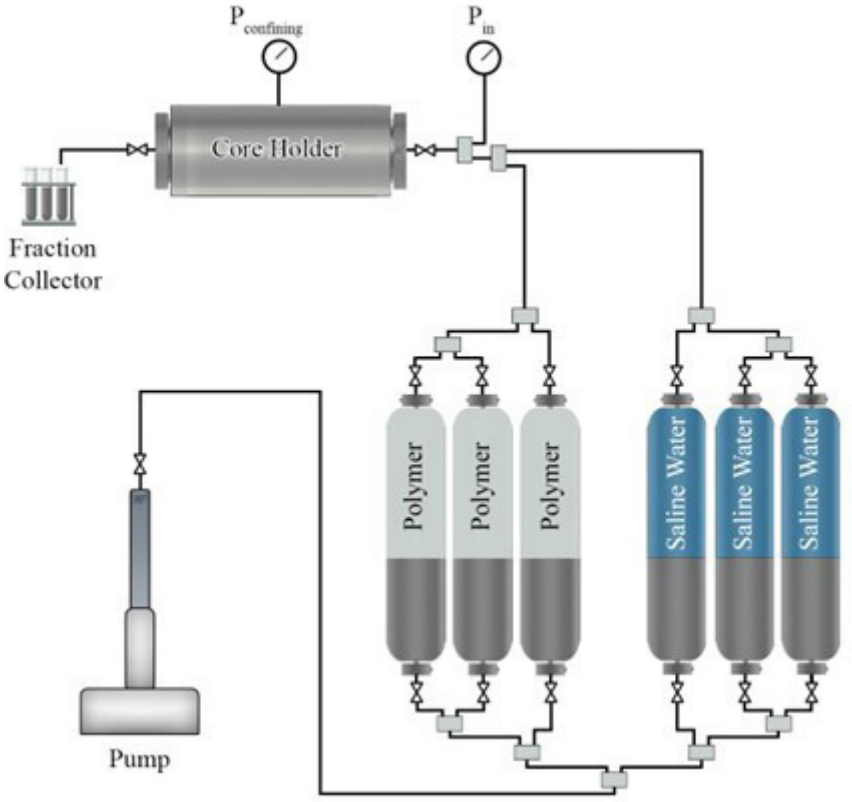

Fig. 2—Coreflood experimental setup.

Composition	Concentration (ppm)
NaCl	124,211
$CaCl_2$	25,8234
$MgCl_2$	8,868
KCl	3,386
$SrCl_2$	592
Total salinity	162,881

Table 1—Synthetic brine composition.

Core Type	Bentheimer
Length (cm)	15.15
Diameter (cm)	3.8
A (cm^2)	11.18
Dry weight (g)	339.34
Pore volume, (cm^3)	41
Porosity (%)	24
Permeability (md)	1,244
Temperature (°C)	Room
Confining pressure (psi)	1,500
Polymer	ZLPAM-40520 1,800 ppm (filtered using 1.2 μm)

Table 2—Core properties and conditions.

In this paper, we commonly use the term "Darcy" velocity (volumetric flow rate per unit of area), which is equivalent to "superficial velocity" or "flux." We recognize that some prefer the use of "interstitial" or "frontal" velocity. Others prefer to convert velocities in porous media to "effective shear rates," so that they may make a direct tie to viscosities measured in a viscometer. We prefer flux/superficial velocity/Darcy velocity because it is an easily measured and definitive quantity. Interstitial/frontal velocity can be easily calculated from flux if porosity and oil saturation are fixed and known. If porosity and especially oil saturation are not precisely known, uncertainty/variability may be introduced. Attempts to convert velocities in porous media to effective shear rates can especially become problematic because there are at least a dozen equations that purport to do this—which can introduce as much as an order of magnitude difference in estimated "shear rate" depending on which conversion equation is used (Cannella et al. 1988; Seright 1991).

Although a wide range of permeabilities exists within the Wara formation, our understanding is that the rheological shift (of resistance factor vs. velocity) in sands and sandstones has been consistently and well demonstrated over many years to be proportional to the square root of permeability divided by porosity and many references therein. Thus, even though our coreflood work was only done in 1,244-md sandstone, previous work provides confidence that the results can be translated to behavior for other permeabilities. In making these statements, we recognize that the level of polymer retention/adsorption can affect resistance factors in porous rock (Vela et al. 1976; Wang et al. 2020)—especially in less-permeable formations (e.g., less than 100 md). We also note that the level of polymer retention/adsorption and its effects on resistance factors tend to be relatively small in very permeable rock (Vela et al. 1976), and we note that most simulators assume that the rheological shift with permeability (mentioned above) is valid (Seright et al. 2023, 2025). Nevertheless, we acknowledge that the safest thing to do for any field application is to measure polymer retention and resistance factors in cores from all formations that are to be flooded with polymer.

Well-A. In this study, we focus our analysis on Well-A in the Wara formation within the Greater Burgan Field. Well-A was perforated at four distinct layers, each exhibiting permeability values that vary more than an order of magnitude (24–659 md) (**Fig. 3** and **Table 3**). Step-rate polymer injection tests were conducted in Well-A and are thoroughly documented in Al-Murayri et al. (2022). As shown in **Table 4**, acid stimulation was performed before polymer injection to reduce wellbore skin. Injection Logging Tool (ILT) measurements were taken at various stages throughout the injectivity tests to assess effective reservoir thickness, fluid distribution across the perforated layers, and conformance improvements during polymer injection. Four ILTs were conducted. The first three were during the waterflood, and the last one (December 2021) involved 1,500-ppm polymer injection at 2,500 barrels per day (bpd). The ILT results showed that over 86% of fluid intake is through the bottom layer. After polymer injection, a slight change in fluid intake was observed within the bottom layer from the December ILT, when compared with the prior ILT during water injection in November 2021 **(Fig. 3)**.

Permeability (md)	Top (ft)	Bottom (ft)	Zone	Perforated Thickness (ft)	ILT (%)
47	4,619	4,628	WU	9	3.5
24	4,632	4,648	WM1	16	5.5
186	4,658	4,662	WM2	4	4.5
659	4,675	4,718	WM3	43	86.5

Table 3—Well log average permeability and ILT fluid intake results from December 2021 during 1,500-ppm polymer injection.

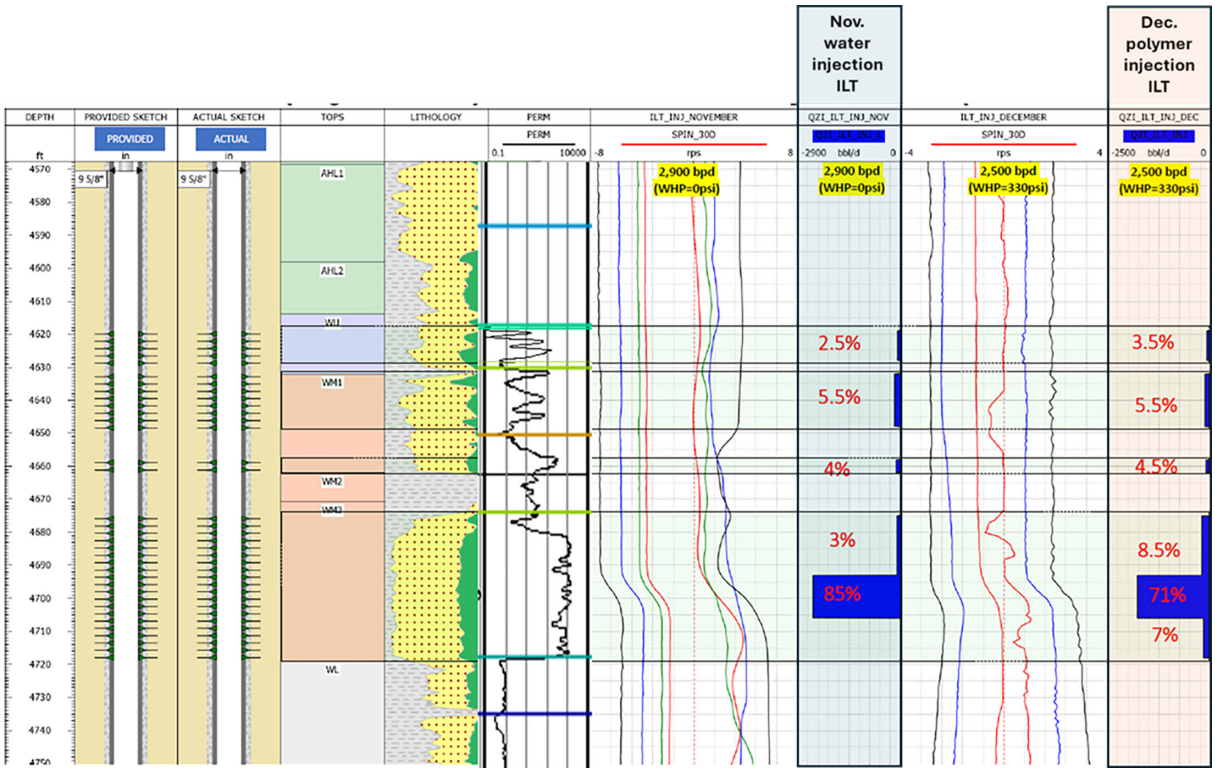

Fig. 3—Well-A well log showing from left to right tracks: ILT, perforation zones, lithology, and permeability for 2021 ILT. November ILT in the blue box shows 88% in the lower zone within two subzones, and December shows a total of 86.5%.

Date(s)	Stage/Event	Notes
18-Aug-2021	ILT	Initial leak test
27-Aug-2021	PFO	Preflush operation
06-Sep-2021	ILT	
13-Oct-2021	Acid stimulation	
14-Oct-2021	Post-acid PFO	
18-Nov-2021	Begin water injection	
26-Nov-2021	PFO	
27-Nov-2021	ILT	Injection rate: 2,900 bbl/day (before first polymer injection)
29-Dec-2021	ILT	Injection rate: 2,500 bbl/day Polymer Conc.: 1,500 ppm (after the fourth polymer injection)

Table 4—Chronological events and injection stages in Well-A.

Additionally, three pressure falloff (PFO) tests were conducted before polymer injection to evaluate formation permeability and the skin factor. Polymer injectivity was assessed using polymer concentrations ranging from 600 to 2,000 ppm and injection rates between 2,000 and 6,000 B/D **(Table 5)**.

Stage	Date(s)	Polymer (ppm)	WHP (psi)	BHP (psi)	Injection Rate (bbl/day)
First polymer injection	3–10 Dec 2021	600	210–430	2,124–2,159	2,000–4,500 (variable)
Second polymer injection	10–17 Dec 2021	900	314–420	2,457–2,579	2,000–6,000
Third polymer injection	17–23 Dec 2021	1,200	314–464	2,457–2,537	2,000–6,000
Fourth polymer injection	23 Dec 2021–14 Feb 2022	1,500	228–364	2,352–2,500	2,000–3,600*
Fifth polymer injection	14–22 Feb 2022	1,800	308–365	2,450–2,500	2,600–3,200
Final injection	22–25 Feb 2022	2,000	320–362	2,460–2,495	2,500–3,100

*Note: The fourth injection stage included variable rates across 14 + dates. See Al-Murayri et al. (2022) for detailed day-wise trends.

Table 5—Polymer injection stages and operating conditions for Well-A.

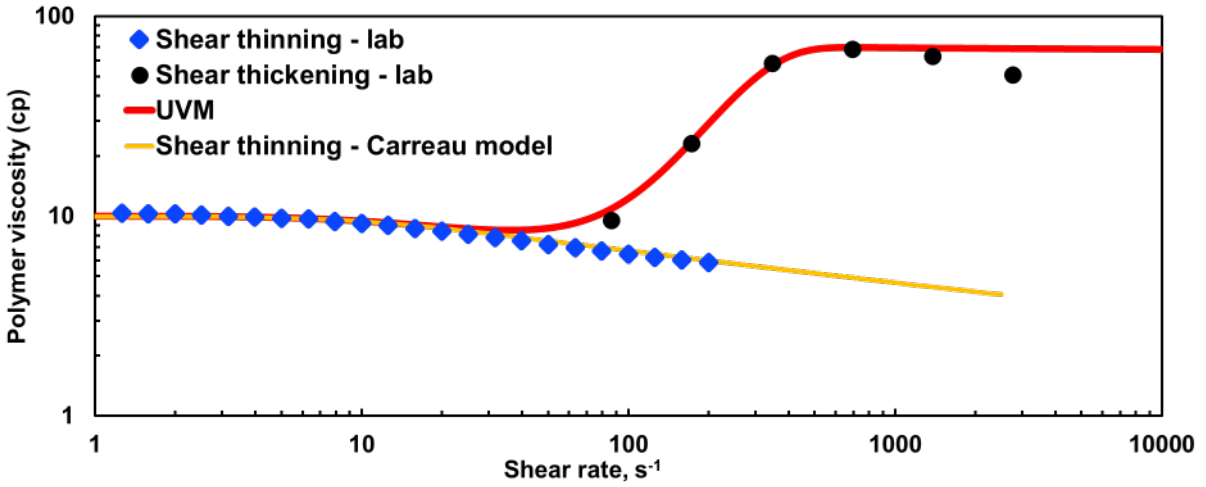

Fig. 4—Laboratory coreflood results for ZLPAM-40520 polymer showing viscoelastic behavior (blue diamonds for shear thinning measured using a viscometer, and black dots are shear thickening measured during coreflooding), while the Carreau model fit in the yellow curve and UVM fit in the red curve.

Injectivity Analysis Interpretation. This study aims to analyze field injectivity measurements by integrating data from recently conducted laboratory experiments with analytical/semianalytical models. Specifically, the results from coreflood experiments will be utilized to characterize the viscoelastic properties of the polymer. These characterizations will enable us to predict the polymer's in-situ behavior using our analytical/semianalytical models described below.

Determine Fracture Initiation Based on Darcy Radial Flow. The first approach involves calculating reservoir injectivity using Darcy's radial flow model and comparing these calculations with injectivity measurements obtained from the field. This comparison serves as a criterion to determine whether the fluid flow adheres to a radial flow pattern or transitions to a linear flow pattern due to fracture propagation. By analyzing the alignment or discrepancies between the modeled and measured injectivity, we can identify the dominant flow regime within the reservoir (Seright et al. 2003). The criterion is defined as such:

$$\left[\frac{q}{\Delta p}\right]_{measured} \gg \left[\frac{\Sigma kh}{141.2\,\mu \ln\left(\frac{r_e}{r_{we}}\right)}\right]_{calculated}. \quad (1)$$

In this equation, q represents the injection or production rate (bpd), Δp is the pressure drawdown (psi), k denotes permeability (md), h is the formation height (ft), μ represents fluid viscosity (cp), and r_e is the external drainage radius (ft) or approximated as half the distance to the nearest well. We account for near-wellbore skin (s) using an equivalent wellbore radius $r_{we} = r_w e^{-s}$, where r_w is the wellbore radius (ft). Skin factor can be obtained from the interpretation of a well-testing method, such as a falloff test. It is worth noting that this criterion follows Darcy's equations assumptions; besides, it assumes that the fluid viscosity fills the whole drainage radius.

Determine Fracture Initiation and Length With UVIM-PKN Model. Abdullah et al. (2023a) presented a semianalytical model to calculate injectivity called the UVIM that accounts for polymer elongational viscosity in the Darcy equation using the unified viscoelastic polymer rheology model (UVM) (Delshad et al. 2008), described as below:

$$\mu_{app} = \mu_\infty + \left(\mu_p^0 - \mu_w\right)\left[1 + \left(\lambda\gamma_{eff}\right)^2\right]^{\frac{n-1}{2}} + \mu_{max}\left[1 - \exp\left(-\left(\lambda_2\tau\gamma_{eff}\right)^{n_2-1}\right)\right], \quad (2)$$

where μ_∞ (cp) is the polymer viscosity at high shear rates is assumed equivalent to water viscosity (μ_w), μ_p^0 (cp) is the polymer viscosity at low shear rates, n is the shear-thinning index, μ_{max} (cp) is the maximum polymer viscosity in shear thickening, n_2 is the shear-thickening exponent, λ is the shear-thinning time constant (seconds), λ_2 is the shear-thickening parameter = 0.01 (unitless) (Zeynalli et al.

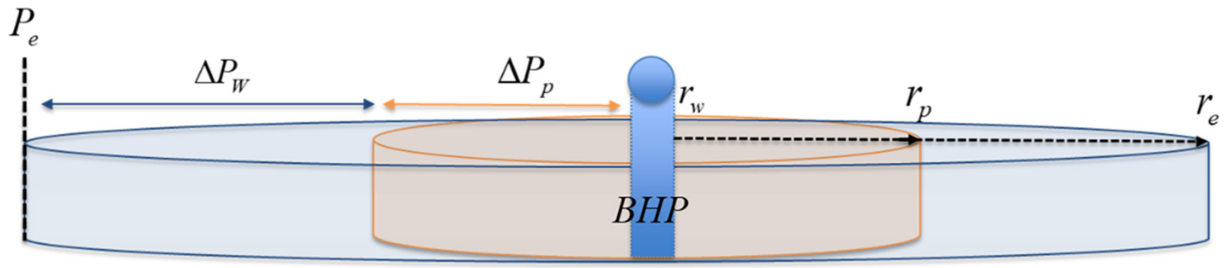

Fig. 5—Schematic diagram of the UVIM conceptual reservoir model. The diagram illustrates the assumption that the reservoir is waterflooded (light blue region) until reaching a steady state and to the residual oil saturation, then the polymer is injected (orange region) (Abdullah et al. 2023a).

2023), and τ approximates the in-situ viscoelastic relaxation time (seconds). The parameters in Eq. 2 are obtained by fitting the UVM flow curve, as shown in **Fig. 4**. Note in Eq. 2 that most of the parameters in the last term (associated with assessing the elongational polymer viscosity) must be determined empirically and experimentally during flow in porous media (e.g., the red curve in **Fig. 4**). Although the "effective shear rate" is included in this last term, it is by no means implied that shear effects cause the elongational viscosity. The effective shear rate γ_{eff} (second^{-1}) in the reservoir is given by (Cannella et al. 1988)

$$\gamma_{eff} = \left[\frac{3n+1}{4n}\right]^{\frac{n}{n-1}} \left[\frac{4CU_r}{\sqrt{8kk_{rw}S_w\phi}}\right], \quad (3)$$

where n is the shear-thinning exponent. C is a correction factor that converts bulk polymer viscosity measured in the viscometer into in-situ polymer rheology. The correction factor is calculated in the laboratory, and it is a function of porosity, permeability, and tortuosity. It can also be obtained by shifting the coreflood measured flow curve to match the bulk rheology flow curve to construct the UVM flow curve (Sorbie 1991; Koh et al. 2018).

And U_r, k, k_{rw}, s_w, and ϕ are the Darcy velocity for radial flow, permeability, water endpoint relative permeability, water saturation, and porosity, respectively.

The UVIM model is coupled with the PKN model, which is a 2D fracture model to predict the fracture length for viscoelastic polymers. UVIM assumes that water is injected into the reservoir until a steady state and residual oil saturation are reached, which is a reasonable assumption, as most of the polymer-thickening behavior occurs around the wellbore, where oil is well swept. Then, the polymer is injected **Fig. 5**. Throughout polymer injection, the BHP of the injection well increases, while the outer boundary pressure (P_e) remains constant (Lake et al. 2014). The total pressure drop (ΔP_T) is the summation of the polymer pressure drop between the wellbore and the extent of the polymer slug (ΔP_p) at r_p, calculated from UVIM, and water zone pressure drop (ΔP_w) from the polymer slug face to the reservoir boundary, calculated from Darcy's law.

$$\Delta P_T = \Delta P_p + \Delta P_w = BHP - P_e. \quad (4)$$

ΔP_p is calculated up to the polymer propagation radius (r_p) based on the UVIM discussed in detail in Abdullah et al. (2023a), and ΔP_w is calculated from r_p to r_e using Eq. 1.

The fracture propagation criteria when coupling the UVIM with PKN shall satisfy the following conditions:

$$BHP > \frac{K_{IC}}{\sqrt{\pi A_f}} + p_f, \quad (5)$$

where bottomhole pressure (BHP) is calculated in Eq. 5 from the UVIM, p_f is the fracture pressure in psi, K_{IC} is the fracture toughness that is related to fracture surface energy [typically 500–2,000 psi.in.$^{0.5}$ (Gidley and Engineers 1989; Economides and Nolte 2000)], and

Shear-Thinning Parameters			Shear-Thickening Parameters		
μ^{∞}	1.1	Infinite shear rate viscosity (cp)	n_2	3.3	Shear-thickening exponent
n	0.8	Shear-thinning index	μ_{max}	65	Max shear-thickening viscosity (cp)
μ_p^0	10	Zero shear rate viscosity (cp)	λ_2	0.01	Shear-thickening parameter
λ	0.1	Shear-thinning time constant (seconds)	τ	0.35	Polymer relaxation time (seconds)

Table 6—UVM parameters used to match lab-measured polymer viscosity.

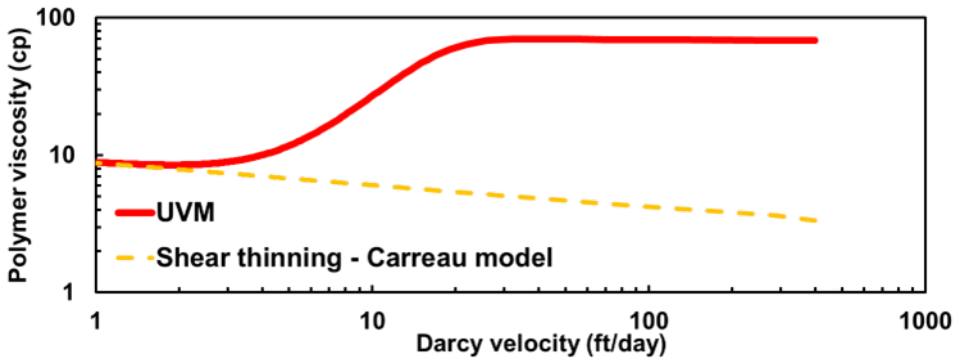

Fig. 6—Calculated in-situ polymer viscosity vs. Darcy velocity for ZLPAM-40520 polymer at 3,200 B/D based on UVM is in the red solid curve, while the Carreau shear-thinning model is in the yellow dashed curve.

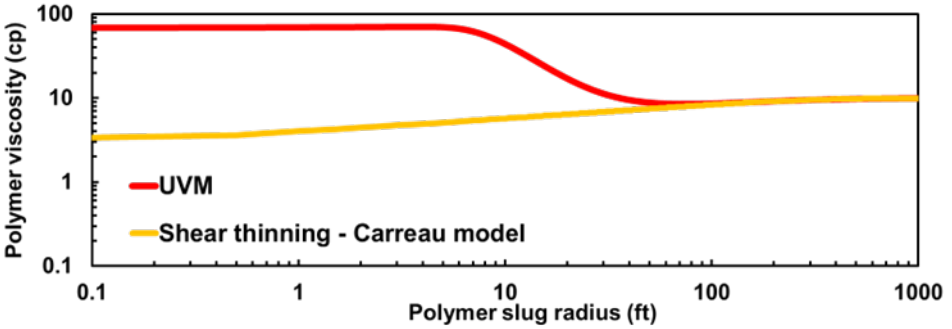

Fig. 7—Calculated in-situ polymer viscosity vs. polymer slug radius for ZLPAM-40520 polymer at 3,200 B/D based on UVM in the red solid line, while the Carreau shear-thinning model is in the yellow curve.

A_f is the fracture geometry parameter (if $2L_f > h_f$, then $A_f = h_f/4$, or if $2L_f < h_f$, then $A_f = L_f$). The fracture pressure and geometry parameter are calculated using the PKN model, as discussed in Abdullah et al. (2023a).

The UVIM-PKN model assumes a constant pressure condition at the reservoir boundary, with the BHP dynamically updated in UVIM using an equivalent wellbore radius as proposed by Prats (1961). The simplified polymer fracture mode (UVIM-PKN) is based on the following assumptions: the reservoir is homogeneous, single-layered, and exhibits single-phase flow, with oil at residual saturation. Flow in a vertical well follows a radial or pseudoradial pattern. The fracture is vertical, bi-winged, and maintains a constant height equivalent to the reservoir thickness. Fluid leakoff from the fracture faces occurs uniformly, and the polymer rheology within the fracture follows a power-law model.

Results and Discussion

Lab Results. The ZLPAM-40520 polymer exhibited viscoelastic behavior when injected at multiple velocities during coreflooding, with a maximum elongational viscosity of 65 cp (black dots in **Fig. 4** and **Table 6**). For the coreflood, we used the resistance factor as an approximation to polymer viscosity, where the resistance factor is the polymer flooding pressure drop divided by the waterflooding pressure drop at each rate. The coreflood results showed shear-thickening behavior when injecting above 6 ft/day **(Fig. 6)**, corresponding to ~30 ft of polymer slug radius. **Fig. 7** illustrates that based on Darcy's radial equation, as the radius increases, the flow velocity (also corresponding to the shear rate in Eq. 3) decreases accordingly. As such, the polymer viscosity is highest at shorter drainage, where the elongational viscosity occurs at higher velocities (effective shear rate in Eq. 2). Thus, from the wellbore to ~30 ft radius, shear thickening is expected to dominate the polymer in-situ rheology, assuming injecting at 3,200 B/D **(Fig. 7)**. This radius value agrees with literature observations for the shear-thickening range of occurrence (Hwang et al. 2019; Seright et al. 2025).

Ideally, our modeling would directly input resistance-factor-vs.-velocity data. However, because substantial effort was made by Abdullah et al. (2023a) and AlAbdullah et al. (2023b) previously to develop the UVIM model, we chose to take advantage of this previous work during the development of our model. Thus, we are required to convert resistance factors into effective viscosities and velocities into shear rates.

Reevaluating Field Injectivity Data. When evaluating the injectivity test results from Al-Murayri et al. (2022), we considered the water injectivity at 4,188 B/D with a BHP of 1,914 psi as a reference water injectivity. In **Fig. 8**, by plotting the actual field polymer injectivity divided by the reference water injectivity at different injection rates. Note that actual injectivity is defined here as the measured injection rate during the polymer injectivity test divided by the pressure difference between the BHP and the average reservoir pressure. Similarly, for water injectivity, we used the values related to water injection duration as a base case. As shown in **Fig. 8**, the injectivity trends for the different polymer concentrations largely overlap, indicating that injectivity changes are only weakly influenced by polymer rheology and are primarily governed by the injection rate. This behavior is expected as the effective injection area increases—similar to fracture extension—and may include minor rheological effects associated with shear-thinning during flow. Such observations led to further investigation using the earlier-mentioned analytical and semianalytical tools.

We regret that viscosity checks were not performed during our field measurements. These should be performed to rule out alternative explanations (e.g., mechanical degradation, near-wellbore dilution/mixing, and completion constraints). Unfortunately, no samples were collected in this case. Also, the operator did not report any measured samples in the field. Sagyndikov et al. (2022) presented an adequate discussion that may aid with these concerns.

Fracture Initiation Based on Darcy Radial Flow. Linear (fracture-like) flow is likely when measured injectivity significantly exceeds the Darcy radial flow injectivity in Eq. 1 (Seright et al. 2003). In other words, the field measure injectivity $\left(\left[\frac{q}{\Delta p}\right]_{measured}\right)$ exceeds the Darcy equation calculated injectivity $\left[\frac{\Sigma kh}{141.2\,\mu \ln\left(\frac{r_e}{r_{we}}\right)}\right]_{calculated}$. As this criterion assumes that the fluid viscosity fills the whole drainage radius (constant viscosity over r_e), plotting the calculated injectivity will result in a constant value for a given drainage radius. Here we will select one drainage radius for each case: e.g., $r_e = 10$ ft in **Fig. 9**. Then, assume that we fill the selected drainage radius with: either (1) water viscosity at 1.1 cp (black line in **Fig. 9**) or (2) polymer viscosity at 1,800 ppm of 10 cp at 7.3 second^{-1} (assumed deep in the reservoir, shown as the blue line in **Fig. 9**), or (3) 65 cp as maximum polymer viscosity due to elongational behavior near the wellbore at 1,000 second^{-1} (shear thickening expected >300 second^{-1} or >20 ft/day from **Fig. 6**) at 1,800 ppm in a thick orange line in **Fig. 9**. Then we calculate the

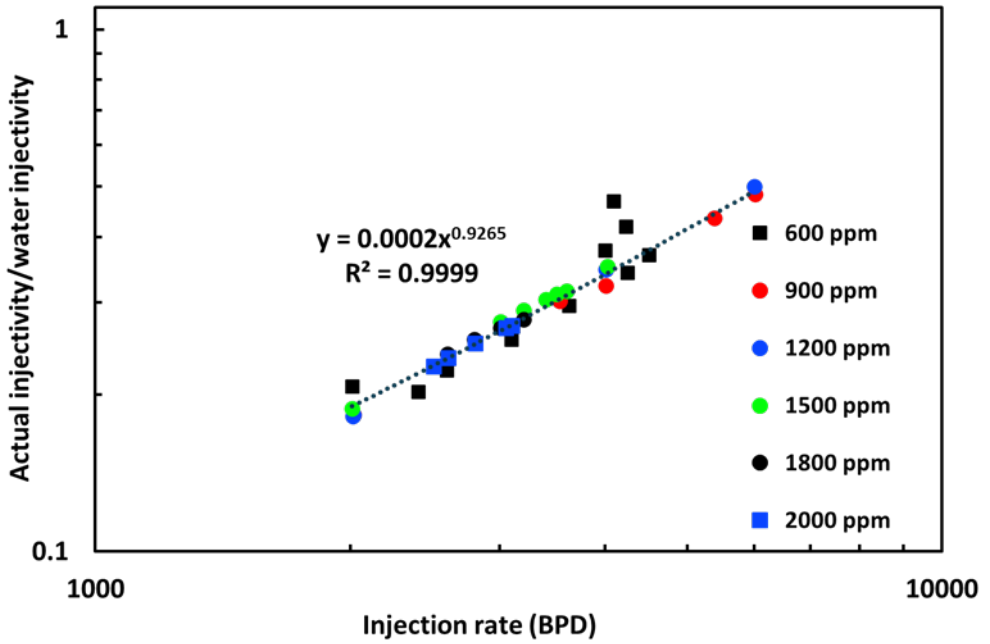

Fig. 8—Actual injectivity divided by the reference water injectivity plotted vs. injection rate at different polymer concentrations.

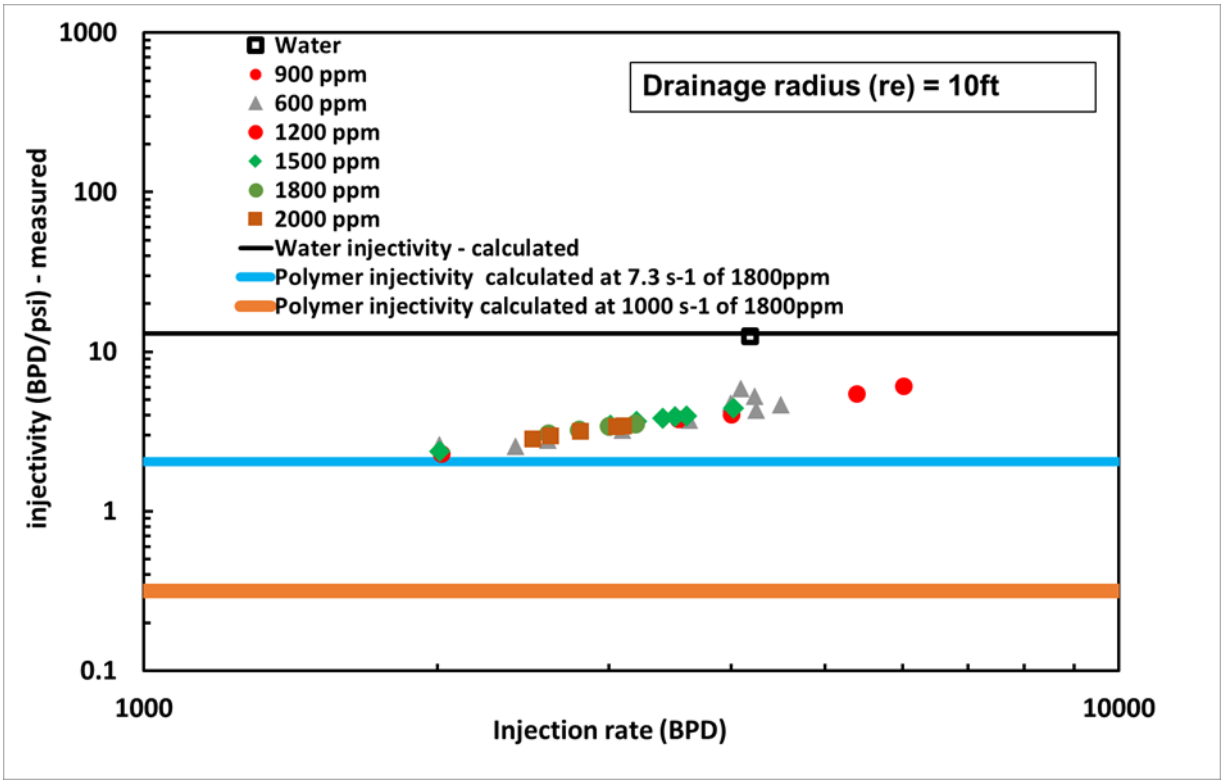

Fig. 9—Comparing polymer measured injectivity from the long-term injectivity tests (in dots) at different concentrations and rates to calculated polymer injectivity (in lines) using Darcy radial equation at a drainage radius of 10 ft.

injectivity using the Darcy equation for the selected drainage diameters and each viscosity using the right-hand side of Eq. 1. After that, we compare the field-measured injectivity with various rates compared with the assumed constant viscosity for the selected drainage radius (see the dots in **Fig. 9**).

As the Darcy radial equation here assumes a single viscosity over the drainage radius, we will vary the drainage radius between 10 ft and 400 ft in **Fig. 9** and **Figs. A-1 through A-3** in Appendix A. This simplified criterion tries to answer how the measure field injectivity

compares with assuming we fill the drainage radius with either water or shear-thinning polymer or an elongated polymer over a drainage radius of 10 ft, 50 ft, 100 ft, and 400 ft.

Only limited information was available from the pressure transient analysis interpretation, and the reported numerical results were not fully traceable. The analyses addressed two stages: before acid stimulation (August 2021), the PFO interpretation indicated a very high skin factor (≈26), consistent with severe near-wellbore damage and restricted injectivity; after acid stimulation (October 2021), the interpreted skin decreased to approximately 12.7, indicating improved near-wellbore flow conditions. However, inconsistencies were observed between these pressure transient analysis-derived parameters and the pressure behavior obtained from reservoir simulations. History matching the field measured injection pressures, by the operator using the reservoir simulator, before and after stimulation, required applying a well-index multiplier of up to ten, which effectively inflates transmissibility and introduces nonuniqueness between *kh* and skin.

To reduce this ambiguity, in this work, we fixed *kh* at 24,580 md·ft based on log-derived permeability and ILT, and the skin factor was estimated by matching stabilized injectivity data from February 2022. Thus, a skin factor of 5 is used to match the calculated injectivity with the measured water injectivity at a reference point of 4,188 bpd (black square overlays the black solid line in **Fig. 9**). As described in Eq. 1, linear flow is expected whenever the measured injectivity exceeds the calculated injectivity for radial flow.

Fig. 9 focuses on the near wellbore region of 10 ft, typically dominated by shear thickening with Darcy velocities ranging from 40 ft/day to 200 ft/day. Injecting above ~1,000 bpd in this region is likely to fracture the well, as it exceeds the threshold indicated by the orange dotted line. **Fig. A-1** (in Appendix A) assumes a conservative scenario in which the polymer reaches only 50 ft at an injection rate of 3,200 B/D within the 43 ft effective target thickness. It demonstrated that injecting at rates above 2,000 bpd leads to fracturing when polymer viscosity is 10 cp without considering shear-thickening effects. **Fig. A-2** shows that at a drainage radius of 100 ft, injecting above 2,000 B/D similarly results in linear flow for a 10 cp polymer viscosity. **Fig. A-3**, based on a 400 ft drainage radius, shows that if there is no shear thickening near the wellbore, the measured polymer viscosity at a shear rate of 7.3 $second^{-1}$ (blue line) indicates linear flow for all polymer concentrations once injection rates exceed ~2,000 bpd. Conversely, linear flow is expected across all concentrations with shear thickening near the wellbore (orange line). This comprehensive analysis underscores the critical injection rates and viscosity conditions necessary to maintain radial flow below the parting pressure. Also, it confirms the occurrence of a fracture during the field injectivity test.

Determine Fracture Initiation and Length With the UVIM-PKN Model. ***Fracture Initiation With UVIM-PKN Model.*** To further confirm our observations, we considered the injected polymer concentration of 1,800 ppm at 2,600–3,200 B/D [the same conditions in the step rate test by Al-Murayri et al. (2022)] and plotted polymer injectivity measured and calculated vs. injection rate **(Fig. 10)**. We calculated injectivity using the UVIM model in three scenarios: shear thinning, following the Carreau (1972) model without fracturing (black triangles); a viscoelastic polymer (shear thinning and thickening) following UVIM but without fracturing (black diamonds); and a viscoelastic polymer with fracture propagation using the UVIM-PKN semianalytical model (red x's). As discussed earlier, UVIM calculates injectivity more accurately than the Darcy radial flow equation, as it accounts for the change in viscosity due to the in-situ change in shear rate in the reservoir.

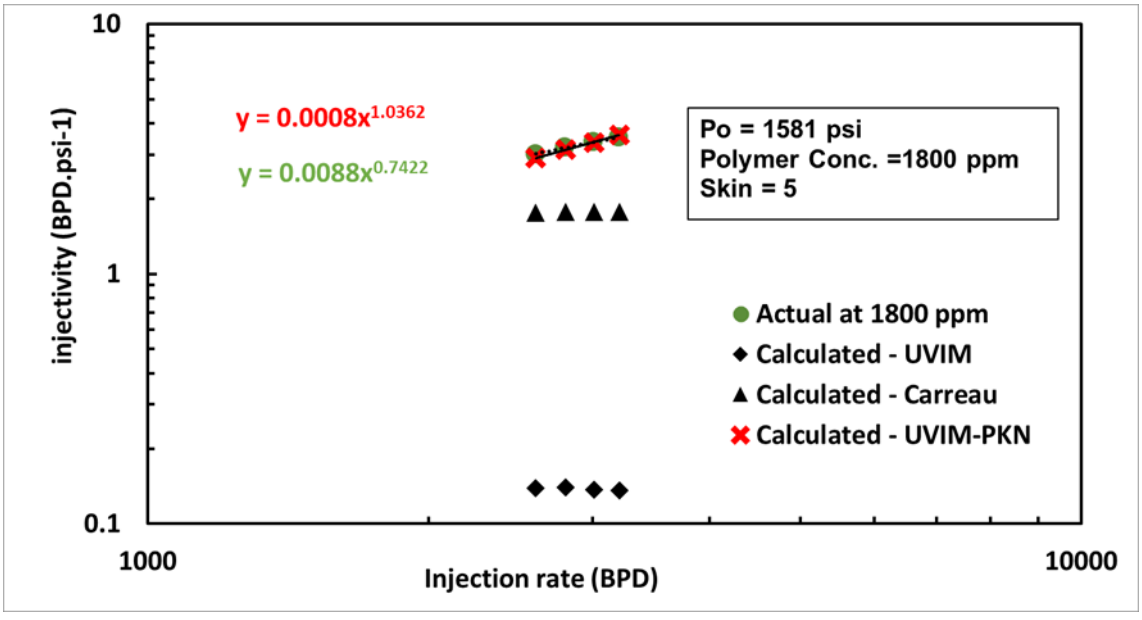

Fig. 10—Measured (green circles) and calculated (black triangles for shear thinning without fracture and black diamonds for viscoelastic polymer without fractures, and red axes for viscoelastic polymer with fracturing) injectivity vs. injection rate at 1,800 ppm polymer concentration.

As expected, when no fractures are assumed, the viscoelastic model (UVIM, black diamonds) predicts lower injectivity than the field-measured values (green circles). This underestimation is attributed to the increased elongational viscosity. In contrast, the Carreau model (black triangles), which assumes shear-thinning behavior but no fractures, aligns more closely with measured injectivity, consistent with polymer rheology in shear-dominated flow such as within fractures (Zechner et al. 2013).

The limited variation in injectivity (in both Carreau and UVIM models) with injection rate is due to the slight variation in the injection rate (between 2,606 and 3,200 B/D) that does not vary polymer viscosity significantly (green and orange lines in **Figs. 11a and 11b**). Because of the limited rate range, we recognize that a convincing extrapolation is challenging. Ideally, a wider range of rates would help.

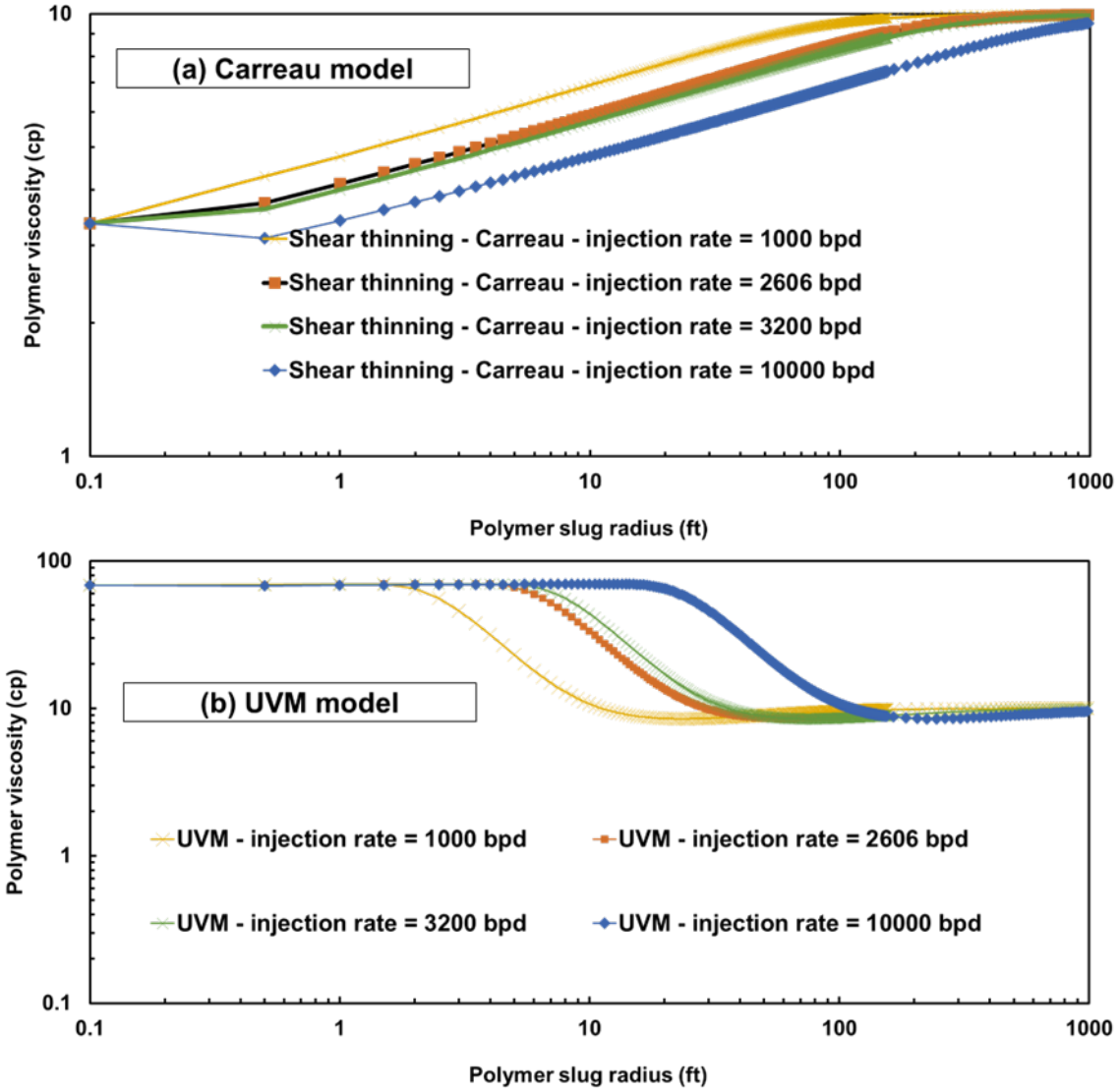

Fig. 11—(a) Shear-thinning Carreau model polymer viscosity vs. polymer propagation radius. (b) Shear-thinning and -thickening UVM model polymer viscosity vs. polymer propagation radius.

Nevertheless, here, we offer our best interpretation with the available data. However, when fracture propagation is explicitly modeled using the UVIM-PKN approach (red x's in **Fig. 10**), injectivity increases more significantly with injection rate than in the Carreau model, which tends to plateau. This trend could suggest an expansion in the injection area due to fracture propagation, as well as a shear-thinning behavior, both of which contribute to improved injectivity. **Table 7** lists the input parameters used for these injectivity calculations. Noting that a shorter slug radius corresponds to proximity to the wellbore, where velocities (and shear rates) are highest. **Fig. 11a** illustrates shear-thinning effects with the Carreau model. The viscosity variation with rate is minor within 1–10 ft (≈3 cp) and contributes little compared with shear thickening, especially near the wellbore. In contrast, the UVM model **(Fig. 11b)** shows viscosity reaching a maximum value (μmax) that plateaus, as also observed in **Fig. 7**. Once the shear rate exceeds a critical value, viscosity rapidly rises and then stabilizes at μmax, producing the observed plateau (illustrated in **Fig. 4**). In **Fig. 11b**, at 3,200 B/D, this plateau extends to ~10 ft, while at higher rates, the elevated velocity persists farther into the reservoir (e.g., ~30 ft at 10,000 B/D vs. ~ 3 ft at 1,000 B/D in **Fig. 11b**). This behavior reflects the logarithmic decline of velocity with radius under Darcy radial flow, consistent with the rheological and modeling framework adopted in this study (Abdullah et al. 2023a, 2023b).

Parameter	Value	Source	Parameter	Value	Source
Injection rate, q (bbl/day)	3,200	Field injectivity test	Water viscosity, μ_w, (cp)	1.1	Laboratory data
Permeability, k (md)	650	Well logs and core data	Polymer concentration, C_p, (wt%)	0.18	Laboratory and field data

Table 7—Parameters used in the injectivity and fracture model UVIM-PKN.

Parameter	Value	Source	Parameter	Value	Source
Formation thickness, h (ft)	43	Well logs and core data	Fracture initiation pressure, p_{fi}	2,500	Step-rate test
Wellbore radius, r_w (ft)	0.3	Well design	Minimum horizontal stress (psi)	2,300	History-matching field BHP. Range can be calculated for a given reservoir pressure, Poisson's ratio, and vertical stress (Eq. 11 in (AlAbdullah et al. 2023b)
Skin factor	5	Well test and injectivity test	Power law exponent, n_p	0.8	Matching polymer bulk rheology with power-law model
Drainage radius, r_e (ft)	400	Half distance from nearest well	Power law parameter, K, (cp·sec$^{(n-1)}$)	16	Matching polymer bulk rheology with power-law model
Boundary Pressure, P_e (psi)	1,581	Well tests and field data	Young's modulus, 'E, (psi)	7,000,000	History-matching field BHP. Typically 500,000–4,300,000 for sandstone with porosity > 16% (Zoback 2010)
Porosity, ϕ (%)	0.18	Well logs and core data	Poisson's ratio, v	0.21	Geomechanics data
Water saturation, S_w (%)	0.7	Well logs and core data	Fracture thickness, h_f, (ft)	43	Assumed = formation thickness
Water endpoint relative permeability, k_{rwo}	0.4	SCAL data	Turbulence parameter, C_{turb}	1.7	(Perkins and Kern 1961; Suri and Sharma 2009; AlAbdullah et al. 2023b).
Correction factor, C	1	Matching bulk and coreflooing polymer viscosity (Koh et al. 2018)	Critical stress intensity factor, K_{IC}, (psi·in.$^{0.5}$)	2,500	History-matching field BHP. Typically 500–2,500 psi·in.$^{0.5}$ (Gidley and Engineers 1989; Economides and Nolte 2000)

Table 7 (continued)—Parameters used in the injectivity and fracture model UVIM-PKN.

Fracture Length With UVIM-PKN Model. As almost all the polymer injection field trials reviewed in the past 43 years indicate fracture initiation in vertical wells, the critical question becomes what is the fracture extension and orientation (Sagyndikov et al. 2022). If fractures extend over one-third of the interwell distance and align toward the producer, the sweep efficiency can be significantly compromised (**Fig. A-4a**). However, if the orientation is perpendicular to the injector producer, we may expect enhancement in injectivity with slower front movement and better sweep efficiency (**Fig. A-4b**) (Dyes et al. 1958; Gadde and Sharma 2001; Lee et al. 2011; Seright 2017).

We history-matched the field BHP at 3,200 bpd and 1,800 ppm between 14 and 22 February 2022. Using the UVIM-PKN model, we calculated a kh value of 24,580 md-ft based on the ILT effective thickness and log-measured permeability **(Table 3)**. We considered a drainage radius of 400 ft, equivalent to half the distance of the actual field well spacing. Prior field injections of lower-concentration polymer were excluded from our calculations. Under these assumptions, the model indicated a fracture half-length of approximately 110 ft—equivalent to one-tenth of the distance between Well-A and its nearest offset well **Fig. 12**. The polymer propagation radius was 123 ft at the end of the injection. The calculated BHP is the result of polymer slug pressure drop and water pressure drop (orange dotted line and blue dashed line in **Fig. 12**), in addition to the boundary pressure of 1,581 psi, as determined using Eq. 4. As illustrated in **Fig. 5**, the polymer slug gradually propagates into the reservoir within a 400-ft boundary. During this process, the pressure drop associated with the polymer slug becomes dominant (orange dotted line in **Fig. 12**), while the water pressure drop correspondingly decreases (blue dashed line in **Fig. 12**). The fracture length extension after the first day results in stabilizing the BHP within the minimum horizontal stress (see Eq. 5). Considering the ILT's effective thickness of 43 ft and elongational viscosity of 65 cp, the injection rate is relatively high, even at a permeability of 650 md. We considered an R_k or residual resistance factor of 1.17 obtained from the falloff test results discussed by Al-Murayri et al. (2022), and consistent with prior studies for such high-permeability rock (Vela et al. 1976; Seright 2017).

Uncertain parameters, including minimum horizontal stress, Young's modulus, and the critical stress intensity factor, were history-matched to reproduce the measured BHP. To evaluate the influence of these tuned parameters on the predicted fracture geometry and pressure response, a sensitivity analysis was performed by systematically varying both the tuned and additional parameters listed in **Table 7**. The corresponding variations in fracture half-length and BHP were computed using the UVIM–PKN model. The range of parameter variation is summarized in **Table 8**. The results indicate that the minimum horizontal stress exerts the strongest control on both fracture half-length and BHP, making it a critical parameter for successful BHP matching **(Fig. 13)**. This could be understood from its role in the UVIM-PKN model as discussed earlier in Eqs. 4 and 5. The permeability reduction factor also showed a pronounced effect on the fracture half-length, which could exceed 100% of the base case when increased to 2, while its impact on BHP remained limited. This behavior can be attributed to the additional pressure drop imposed by R_k near the wellbore, which is compensated by fracture extension such that the stabilized BHP approaches the minimum horizontal stress, as governed by Eqs. 4 and 5. Other parameters, such as Young's Modulus, turbulence parameters, and critical intensity factor, exhibited a moderate to low impact on the BHP and fracture half-length within the selected parameter boundaries **(Fig. 13)**.

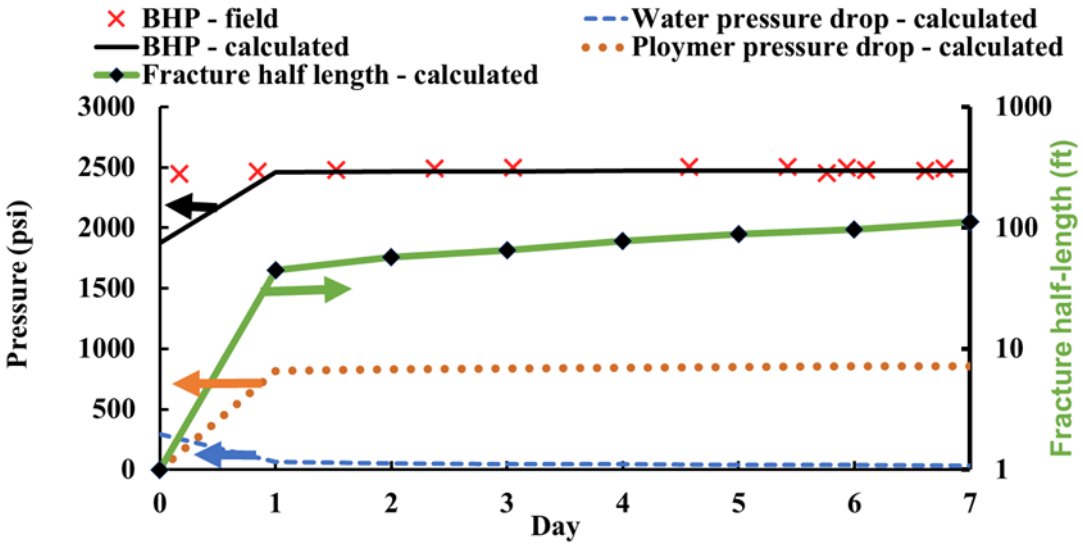

Fig. 12—History-matching the field BHP (red x's) with UVIM-PKN model (black solid line), resulting in fracture half-length of ~110 ft (green solid lines on the right y-axis). The orange dotted and blue dashed lines represent the calculated polymer propagation pressure drop and water pressure drop. The summation of both lines with the boundary pressure of 1,581 psi results in the calculated BHP in the black solid line using Eq. 4.

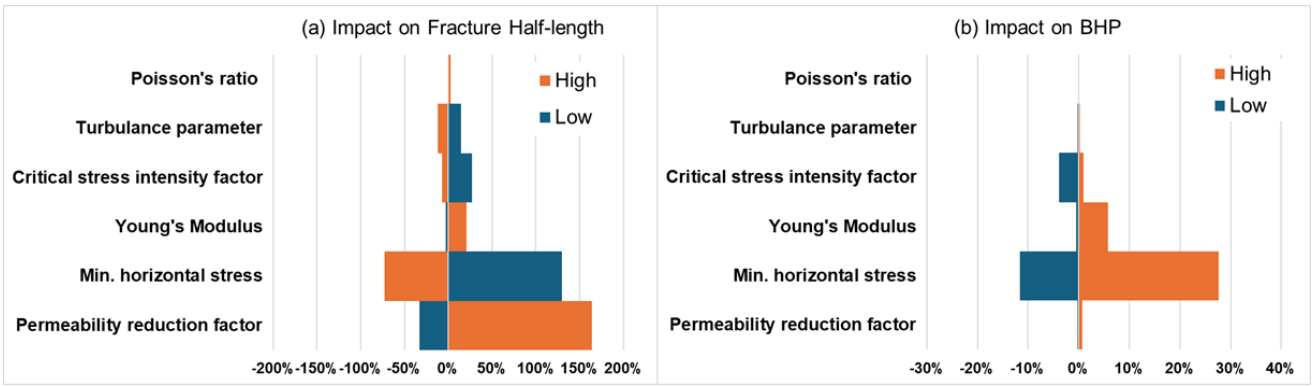

Fig. 13—(a) and (b) Impact of varying the sensitivity parameters on fracture half-length and calculated BHP reservoir, in comparison with the history-matched base case.

Parameter	Low	Base Case (History-Matched)	High
Permeability reduction factor	1	1.17	2
Min. horizontal stress (psi)	2,000	2,300	3,000
Young's modulus	500,000	700,000	4,300,000
Critical stress intensity factor (psi·in.$^{0.5}$)	500	2,500	3,000
Turbulence parameter	1	1.7	2
Poisson's ratio	0.1	0.21	0.3

Table 8—Values of sensitivity parameters compared with the history-matched base case.

Although falloff tests were conducted at Well-A, their early-time data were of poor quality, and it was challenging to interpret fracture occurrence and length. Also, the falloff tests were conducted only during the waterflooding period. Considering that in the Wara formation, the nearest well is roughly 800 ft away from Well-A and the maximum stress is oriented along the NW-SE direction, field operators can examine whether fracture extension will enhance, impair, or have minimal impact on large-scale polymer injection. High-quality falloff tests conducted after the planned polymer injection could verify the extent of fracture propagation. In addition, combining these well tests with further geomechanical measurements—such as minimum horizontal stress magnitude and other rock properties—will help to monitor fracture growth accurately.

Implications of Polymer Field Expansion Strategy. The goal of switching from waterflooding to polymer flooding should be well-defined. The lower formation in Wara **(Fig. 3)** showed that even after polymer flooding, ~90%°F the injection intake was into the bottom high-permeability layer. However, a slight redistribution within the bottom layer is observed after polymer flooding, which could be due to different interpretations by the vendors who acquired the data. When calculating the endpoints' mobility ratio, it is 0.25, assuming an oil viscosity of 3 cp, a polymer viscosity of 4.7–10 cp [targeted polymer viscosity for full-field (Al-Qattan et al. 2024)], and the water and oil endpoints of 0.4 and 1, respectively. These values result in a favorable ratio (i.e., below unity), but considering the high permeability ratio between the bottom layers and the other layers (ranging from 4 to 27 between the various layers, **Table 3**), a mobility ratio reduction to 0.03 (polymer viscosity of 40 cp) is needed to overcome the conformance across the layers (Seright 2017). Injection of a polymer at this viscosity might be operationally challenging due to injectivity restrictions and the potential for excessive fracture extension. In such a case, other conformance control strategies should be considered. Certainly, cases exist where wide fractures or fracture-like features cause direct and severe channeling between injectors and producers. A wide range of conformance improvement options is available for such circumstances. Please refer to Seright and Brattekas (2021) for a discussion of the available options. Some of these options include (1) gel treatments to block parts of the fracture, (2) reduced rates or polymer viscosity in hopes that in-situ stresses may close the fracture naturally, (3) reconfiguring injection and/or production wells to align the flooding pattern to be perpendicular to the direction that fractures or fracture-like features naturally grow (Seright and Wang 2023), and (4) specialized completions (e.g., inflow-control devices) for circumstances where entry into the fracture can be isolated at the wellbore (e.g., vertical fractures crossing a horizontal well).

Summary and Conclusions

Analytical models, including Darcy radial flow and the viscoelastic injectivity model (UVIM), were used to evaluate the onset of nonradial flow and fracture initiation. The results indicate that fracture-like flow is observed at polymer concentrations of 1,800 ppm and injection rates exceeding 2,000 B/D. Additionally, the UVIM-PKN model, validated against field data, predicts fracture propagation trends, showing that fracture half-lengths can extend up to 90 ft, approximately one-tenth of the distance to the nearest offset well. The findings of this study can be listed as follows:

1. If no fractures or fracture-like features existed and severe mechanical degradation of the polymer did not occur, significant injectivity loss would have been observed during polymer flooding in the Wara formation as a result of polymer viscoelasticity. The absence of such injectivity losses suggests that fractures or fracture-like features likely developed during polymer injection.
2. Laboratory and analytical models' results indicate that nonradial (fracture-like) flow dominates at high polymer concentrations and injection rates exceeding 2,000 B/D.
3. By matching field injectivity data, the UVIM-PKN model predicts fracture propagation extending approximately 90 ft within the Wara formation.
4. Fracture orientation plays a crucial role in polymer sweep efficiency, with perpendicular fractures benefiting injectivity while minimizing the negative impact on displacement efficiency.
5. Further assessment of the purpose of polymer flooding is needed for the Wara formation, as insignificant conformance enhancement is observed, with a permeability contrast reaching 27 times between the layers.
6. Conformance control with polymer flooding might require injecting up to 40 cp polymer to overcome the permeability contrast, which could be infeasible.
7. High-quality falloff tests and further geomechanical assessments are necessary to accurately monitor fracture growth and optimize large-scale polymer injection strategies, especially after polymer injection.

Nomenclature

a = relative capacity parameter, unitless
A_f = fracture geometry parameter, ft
BHP = bottomhole pressure, psi, [Pa]
C = insitu shear rate correction factor
C_p = polymer concentration, wt%
C_{Turb} = correction coefficient for turbulence effect, unitless
C_{SEP} = effective salinity, meq·mL-1
E = Young's Modulus, psi [Pa]
F_{CD} = fracture conductivity, unitless
h = reservoir thickness, ft [m]
h_f = fracture height, ft
k = permeability, md [m^2]
k_f = fracture permeability, darcys [μm^2]
k_p = polymer permeability, md [m^2]
k_{rw} = water relative permeability, unitless
k_w = water permeability, md, [m^2]
K = power-law coefficient, psi·sec $^{n-1}$
K_{IC} = fracture toughness, psi·$inch^{0.5}$
Mw = molecular weight, Mg/mol [M Daltons]
n = shear-thinning index, unitless
n_2 = exponent associated with the shear-thickening behavior, unitless
n_p = power-law exponent, unitless
P_e = boundary pressure, psi
$P_{net(\max)}$ = maximum fracture net pressure, psi [Pa]
P_f = fracture pressure, psi [Pa]
P_{fi} = fracture initiation or breakdown pressure, psi [Pa]
P_{res} = pore or reservoir pressure, psi [Pa]
P_{tip} = pressure at the fracture tip, psi [Pa]
q = injection rate, [m^3/sec]
r_e = boundary radius, ft [m]

r_p = polymer slug radius, ft [m]
r_{wD} = dimensionless effective wellbore radius, unitless
r_{we} = equivalent wellbore radius, ft [m]
R_k = permeability reduction factor, unitless
s_p = polymer salinity slope, unitless
S_w = water saturation, unitless
S_{orw} = residual oil saturation, unitless
T = temperature, °F [°K]
U_r = Darcy velocity, ft/day [m/sec]
x_f = distance from the wellbore to an arbitrary point along the fracture, ft [m]
$\bar{w}_f$ = average fracture width, ft [m]
$w_{f\max}$ = maximum fracture width, ft [m]
τ = approximates in-situ viscoelastic relaxation time, seconds
μ_{max} = maximum polymer viscosity in shear thickening, cp [mPa s]
λ_2 = shear-thickening parameter = 0.01, unitless
$\hat{\lambda}$ = shear-thinning time constant, sec
ν = Poisson's ratio, unitless
ΔP_T = total pressure drop, psi [Pa]
ΔP_p = polymer pressure drop, psi [Pa]
ΔP_w = water pressure drop, psi [Pa]
μ_{app} = apparent polymer viscosity, cp [mPa s]
μ_∞ = polymer viscosity at high shear rate, cp [mPa s]
μ_p = polymer viscosity, cp [mPa s]
μ_w = water viscosity, cp [mPa s]
μ_p^0 = zero-shear rate polymer viscosity, cp [mPa s]
$\sigma_{h\max}$ = are maximum horizontal stress, psi [Pa]
$\sigma_{h\min}$ = minimum horizontal stress, psi [Pa]
γ_{eff} = effective shear rate in the reservoir, sec^{-1}
β_p = fitting parameter describing divalent to anions effectiveness, dimensionless
φ = porosity, unitless
$\dot{\gamma}$ = shear rate, sec^{-1}

Acknowledgments

The authors acknowledge Kuwait Oil Co.'s management for granting permission to publish this work and the Enhanced Oil Recovery Center at Kuwait University project number GE01/17 for facilitating the laboratory experiments.

References

Abdullah, M. B., Baqer, S., Delshad, M. et al. 2023a. Unified Viscoelastic Injectivity Model: Analytical Solutions Predicting Polymer Excess Pressure and Fracture Initiation. *Geoenergy Sci Eng* **221**: 111259. https://doi.org/10.1016/j.petrol.2022.111259.

AlAbdullah, M. B., Seright, R. S., Machado, M. V. B. et al. 2023b. An Analytical Tool to Predict Fracture Extension and Elastic Desaturation for Polymer Field Projects. Paper presented at the SPE Annual Technical Conference and Exhibition, San Antonio, Texas, USA, 16−18 October. https://doi.org/10.2118/215083-MS.

Al-Murayri, M. T., Al-Qattan, A., Hassan, A. A. et al. 2022. First Polymer Injectivity Test in the Wara Formation of the Great Burgan Field: Strategic Milestone to Fast-Track Phased Commercial Polymer-Flooding Development. Paper presented at the ADIPEC, 31 October–3 November. https://doi.org/10.2118/211427-MS.

Al-Murayri, M. T., Kamal, D. S., Al-Qattan, A. et al. 2021. A Practical and Economically Feasible Surfactant EOR Strategy: Impact of Injection Water Ions on Surfactant Utilization. *J Pet Sci Eng* **201**: 108479. https://doi.org/10.1016/j.petrol.2021.108479.

Al-Qattan, A., Al-Murayri, M., Almahmid, N. et al. 2024. First Long-Term Polymer Injectivity (LTPI) Test in Magwa Field Targeting Medium Quality Formation in Wara, Great Burgan Field. Paper presented at the International Petroleum Technology Conference, Dhahran, Saudi Arabia, 12−13 February. https://doi.org/10.2523/IPTC-24064-MS.

Azad, M. S. 2023. Characterization of Nonlinear Viscoelastic Properties of Enhanced Oil Recovery Polymer Systems Using Steady-Shear Rheometry. *SPE J.* **28** (2): 664–682. https://doi.org/10.2118/212824-PA.

Cannella, W. J., Huh, C., and Seright, R. S. 1988. Prediction of Xanthan Rheology in Porous Media. Paper presented at the SPE Annual Technical Conference and Exhibition, Houston, Texas, USA, 2−5 October. https://doi.org/10.2118/18089-MS.

Carreau, P. J. 1972. Rheological Equations from Molecular Network Theories. *Trans Soc Rheol* **16** (1): 99–127. https://doi.org/10.1122/1.549276.

Chauveteau, G. 1981. Molecular Interpretation of Several Different Properties of Flow of Coiled Polymer Solutions Through Porous Media in Oil Recovery Conditions. Paper presented at the SPE Annual Technical Conference and Exhibition, San Antonio, Texas, USA, 4−7 October. https://doi.org/10.2118/10060-MS.

Clemens, T., Deckers, M., Kornberger, M. et al. 2013. Polymer Solution Injection – Near Wellbore Dynamics and Displacement Efficiency, Pilot Test Results, Matzen Field, Austria. Paper presented at the EAGE Annual Conference & Exhibition Incorporating SPE Europec, London, UK, 10−13 June. https://doi.org/10.2118/164904-MS.

Dandekar, A., Bai, B., Barnes, J. et al. 2021. Heavy Oil Polymer EOR in the Challenging Alaskan Arctic - It Works! Paper presented at the SPE/AAPG/SEG Unconventional Resources Technology Conference, Houston, Texas, USA, 26−28 July. https://doi.org/10.15530/urtec-2021-5077.

Delshad, M., Kim, D. H., Magbagbeola, O. A. et al. 2008. Mechanistic Interpretation and Utilization of Viscoelastic Behavior of Polymer Solutions for Improved Polymer-Flood Efficiency. Paper presented at the SPE Symposium on Improved Oil Recovery, Tulsa, Oklahoma, USA, 20−23 April. https://doi.org/10.2118/113620-MS.

Dupas, A., Hénaut, I., Rousseau, D. et al. 2013. Impact of Polymer Mechanical Degradation on Shear and Extensional Viscosities: Towards Better Injectivity Forecasts in Polymer Flooding Operations. Paper presented at the SPE International Symposium on Oilfield Chemistry, The Woodlands, Texas, USA, 8−10 April. https://doi.org/10.2118/164083-MS.

Dyes, A. B., Kemp, C. E., and Caudle, B. H. 1958. Effect of Fractures on Sweep-out Pattern. *Trans AIME* **213** (1): 245–249. https://doi.org/10.2118/1071-G.

Economides, M. J. and Nolte, K. G. 2000. *Reservoir Stimulation*. Hoboken, New Jersey, USA: Wiley.

Erincik, M. Z., Qi, P., Balhoff, M. T. et al. 2018. New Method To Reduce Residual Oil Saturation by Polymer Flooding. *SPE J.* **23** (5): 1944–1956. https://doi.org/10.2118/187230-PA.

Filak, J.-M., Al-Houti, R. A., Dashti, L. et al. 2017. Object-Based Modeling of Wara Formation Middle Cretaceous in Greater Burgan Field: An Innovative Approach for a Better Reservoir Characterization. Paper presented at the SPE Kuwait Oil & Gas Show and Conference, Kuwait City, Kuwait, 15−18 October. https://doi.org/10.2118/187645-MS.

Gadde, P. B. and Sharma, M. M. 2001. Growing Injection Well Fractures and Their Impact on Waterflood Performance. Paper presented at the SPE Annual Technical Conference and Exhibition, New Orleans, Louisiana, 30 September–3 October. https://doi.org/10.2118/71614-MS.

Gidley, J. L. and Engineers, S. 1989. *Recent Advances in Hydraulic Fracturing*. Henry L. Doherty Memorial Fundof AIME, Society of Petroleum Engineers.

Glasbergen, G., Wever, D., Keijzer, E. et al. 2015. Injectivity Loss in Polymer Floods: Causes, Preventions and Mitigations. Paper presented at the SPE Kuwait Oil and Gas Show and Conference, Mishref, Kuwait, 11−14 October. https://doi.org/10.2118/175383-MS.

Hwang, J., Sharma, M., Chiotoroiu, M.-M. et al. 2019. Viscoelastic Polymer Injectivity: A Novel Semi-Analytical Simulation Approach and Impact of Induced Fractures and Horizontal Wells. Paper presented at the SPE Annual Technical Conference and Exhibition, Calgary, Alberta, Canada, 30 September–2 October. https://doi.org/10.2118/195978-MS.

Koh, H., Lee, V. B., and Pope, G. A. 2018. Experimental Investigation of the Effect of Polymers on Residual Oil Saturation. *SPE J.* **23** (1): 1–17. https://doi.org/10.2118/179683-PA.

Lake, L., Johns, R. T., Rossen, W. R. et al. 2014. Fundamentals of Enhanced Oil Recovery. *SPE J.*. https://doi.org/10.2118/9781613993286.

Lee, K., Huh, C., and Sharma, M. M. 2011. Impact of Fracture Growth on Well Injectivity and Reservoir Sweep during Waterflood and Chemical EOR Processes. Paper presented at the SPE Annual Technical Conference and Exhibition, Denver, Colorado, USA, 30 October–2 November. https://doi.org/10.2118/146778-MS.

Manichand, R. N. N., Moe Soe Let, K. P. P., Gil, L. et al. 2013. Effective Propagation of HPAM Solutions Through the Tambaredjo Reservoir During a Polymer Flood. *SPE Prod & Oper* **28** (4): 358–368. https://doi.org/10.2118/164121-PA.

Melo, M. A., Lins, A. G., and Silva, I. P. G. 2017. Lessons Learned From Polymer Flooding Pilots in Brazil. Paper presented at the SPE Latin America and Caribbean Mature Fields Symposium, Salvador, Bahia, Brazil, 15−16 March. https://doi.org/10.2118/184941-MS.

Perkins, T. K. and Kern, L. R. 1961. Widths of Hydraulic Fractures. *J Pet Technol* **13** (9): 937–949. https://doi.org/10.2118/89-PA.

Prats, M. 1961. Effect of Vertical Fractures on Reservoir Behavior-Incompressible Fluid Case. *SPE J.* **1** (2): 105–118. https://doi.org/10.2118/1575-G.

Qi, P., Ehrenfried, D. H., Koh, H. et al. 2017. Reduction of Residual Oil Saturation in Sandstone Cores by Use of Viscoelastic Polymers. *SPE J.* **22** (2): 447–458. https://doi.org/10.2118/179689-PA.

Sagyndikov, M., Seright, R., Kudaibergenov, S. et al. 2022. Field Demonstration of the Impact of Fractures on Hydrolyzed Polyacrylamide Injectivity, Propagation, and Degradation. *SPE J.* **27** (02): 999–1016. https://doi.org/10.2118/208611-PA.

Seright, R. S. 1983. The Effects of Mechanical Degradation and Viscoelastic Behavior on Injectivity of Polyacrylamide Solutions. *SPE J.* **23** (3): 475–485. https://doi.org/10.2118/9297-PA.

Seright, R. S. 1991. Effect of Rheology on Gel Placement. *SPE Res Eng* **6** (2): 212–218. https://doi.org/10.2118/18502-PA.

Seright, R. S. 2017. How Much Polymer Should Be Injected During a Polymer Flood? Review of Previous and Current Practices. *SPE J.* **22** (1): 1–18. https://doi.org/10.2118/179543-PA.

Seright, R. and Brattekas, B. 2021. Water Shutoff and Conformance Improvement: An Introduction. *Pet Sci* **18** (2): 450–478. https://doi.org/10.1007/s12182-021-00546-1.

Seright, R. S. and Wang, D. 2023. Polymer Flooding: Current Status and Future Directions. *Pet Sci* **20** (2): 910–921. https://doi.org/10.1016/j.petsci.2023.02.002.

Seright, R. S., Seheult, J. M., and Talashek, T. 2009. Injectivity Characteristics of EOR Polymers. *SPE Res Eval & Eng* **12** (5): 783–792. https://doi.org/10.2118/115142-PA.

Seright, R. S., Lane, R. H., and Sydansk, R. D. 2003. A Strategy for Attacking Excess Water Production. *SPE Prod & Fac* **18** (3): 158–169. https://doi.org/10.2118/84966-PA.

Seright, R. S., Jouenne, S., and Aften, C. 2025. Effect of Salinity and Hardness on HPAM Rheology in Sandstone. Paper presented at the SPE International Conference on Oilfield Chemistry, Galveston, Texas, USA, 9−10 April. https://doi.org/10.2118/224231-MS.

Seright, R. S., Azad, M. S., AlAbdullah, M. B. et al. 2023. Effect of Residual Oil Saturation and Salinity on HPAM Rheology in Porous Media. Paper presented at the SPE Annual Technical Conference and Exhibition, San Antonio, Texas, USA, 16−18 October. https://doi.org/10.2118/215060-MS.

Sorbie, K. S. 1991. *Polymer-Improved Oil Recovery*. USA: Springer Science & Business Media. https://doi.org/10.1007/978-94-011-3044-8.

Southwick, J. G. and Manke, C. W. 1988. Molecular Degradation, Injectivity, and Elastic Properties of Polymer Solutions. *SPE Res Eng* **3** (4): 1193–1201. https://doi.org/10.2118/15652-PA.

Suri, A. and Sharma, M. M. 2009. Fracture Growth in Horizontal Injectors. Paper presented at the SPE Hydraulic Fracturing Technology Conference, The Woodlands, Texas, 19−21 January. https://doi.org/10.2118/119379-MS.

Vela, S., Peaceman, D. W., and Sandvik, E. I. 1976. Evaluation of Polymer Flooding in a Layered Reservoir With Crossflow, Retention, and Degradation. *SPE J.* **16** (2): 82–96. https://doi.org/10.2118/5102-PA.

Wang, D., Han, P., Shao, Z. et al. 2008. Sweep-Improvement Options for the Daqing Oil Field. *SPE Res Eval & Eng* **11** (1): 18–26. https://doi.org/10.2118/99441-PA.

Wang, D., Li, C., and Seright, R. S. 2020. Laboratory Evaluation of Polymer Retention in a Heavy Oil Sand for a Polymer Flooding Application on Alaska's North Slope. *SPE J.* **25** (4): 1842–1856. https://doi.org/10.2118/200428-PA.

Zechner, M., Buchgraber, M., Clemens, T. et al. 2013. Flow of Polyacrylamide Polymers in the Near-Wellbore-Region, Rheological Behavior within Induced Fractures and Near-Wellbore Area. Paper presented at the SPE Annual Technical Conference and Exhibition, New Orleans, Louisiana, USA, 30 September–2 October 2. https://doi.org/10.2118/166085-MS.

Zechner, M., Clemens, T., Suri, A. et al. 2015. Simulation of Polymer Injection Under Fracturing Conditions—An Injectivity Pilot in the Matzen Field, Austria. *SPE Res Eval & Eng* **18** (2): 236–249. https://doi.org/10.2118/169043-PA.

Zeynalli, M., Al-Shalabi, E. W., and AlAmeri, W. 2023. An Extended Unified Viscoelastic Model for Predicting Polymer Apparent Viscosity at Different Shear Rates. *SPE Res Eval & Eng* **26** (1): 99–121. https://doi.org/10.2118/206010-PA.

Zoback, M. D. 2010. *Reservoir Geomechanics*. Cambridge, United Kingdom: Cambridge University Press.

Appendix A

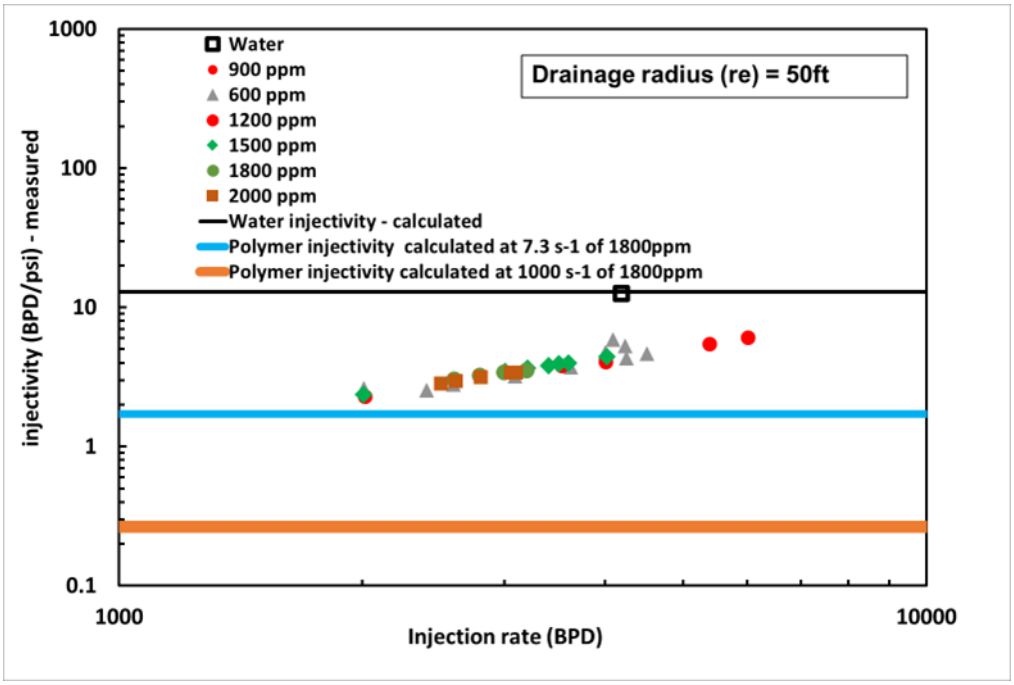

Fig. A-1—Comparing polymer measured injectivity from the long-term injectivity tests (in dots) at different concentrations and rates to calculated polymer injectivity (in lines) using the Darcy radial equation at various drainage radii of 50 ft.

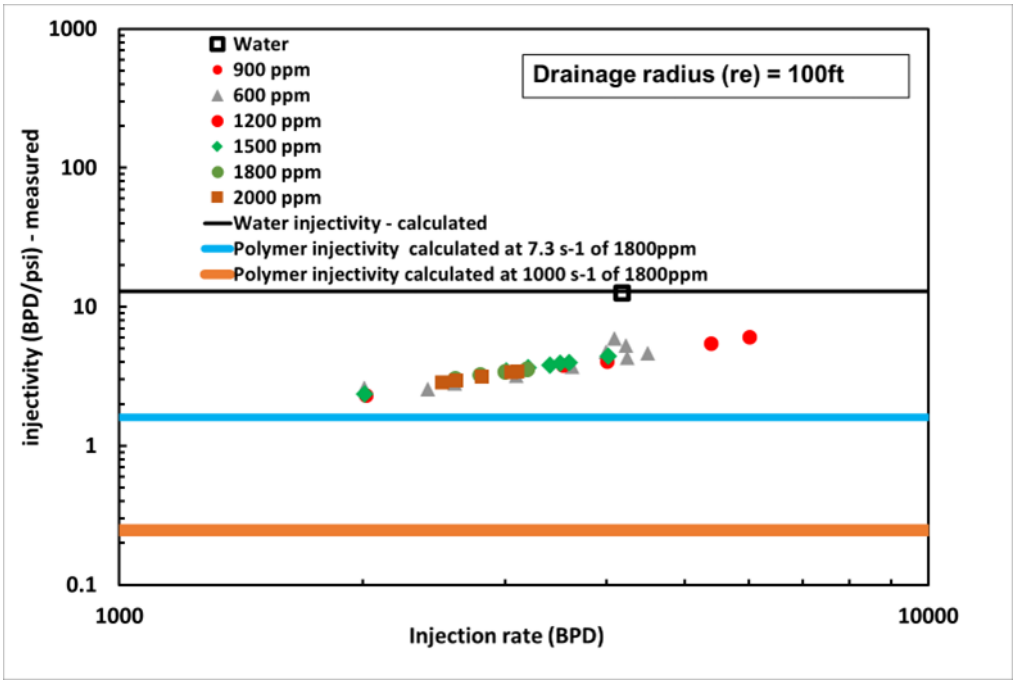

Fig. A-2—Comparing polymer measured injectivity from the long-term injectivity tests (in dots) at different concentrations and rates to calculated polymer injectivity (in lines) using the Darcy radial equation at various drainage radii of 100 ft.

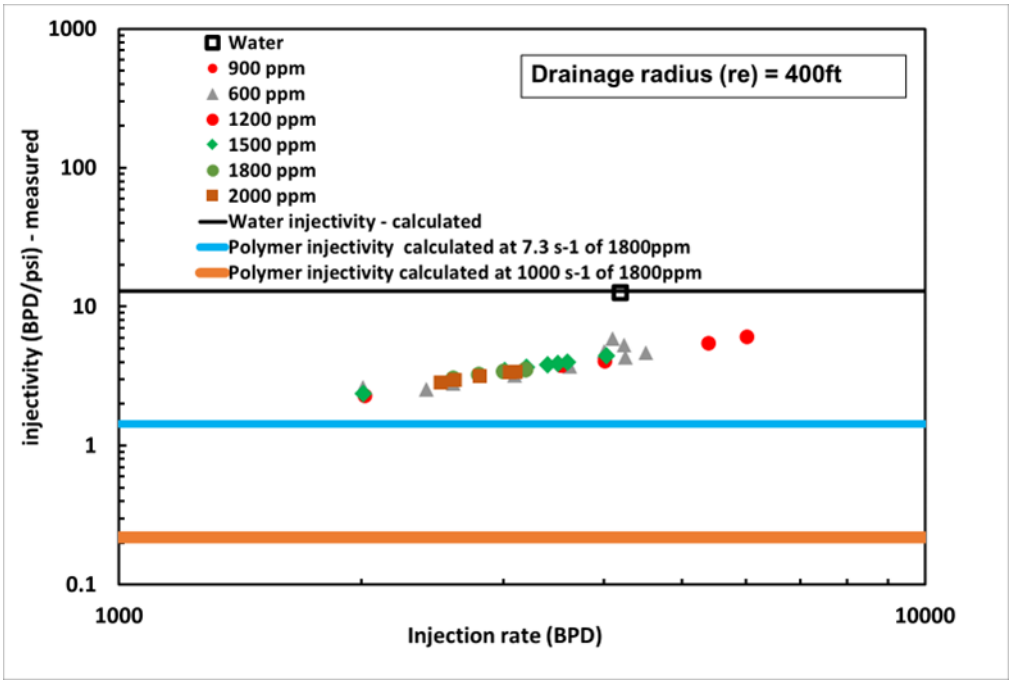

Fig. A-3—Comparing polymer measured injectivity from the long-term injectivity tests (in dots) at different concentrations and rates to calculated polymer injectivity (in lines) using the Darcy radial equation at various drainage radii of 400 ft.

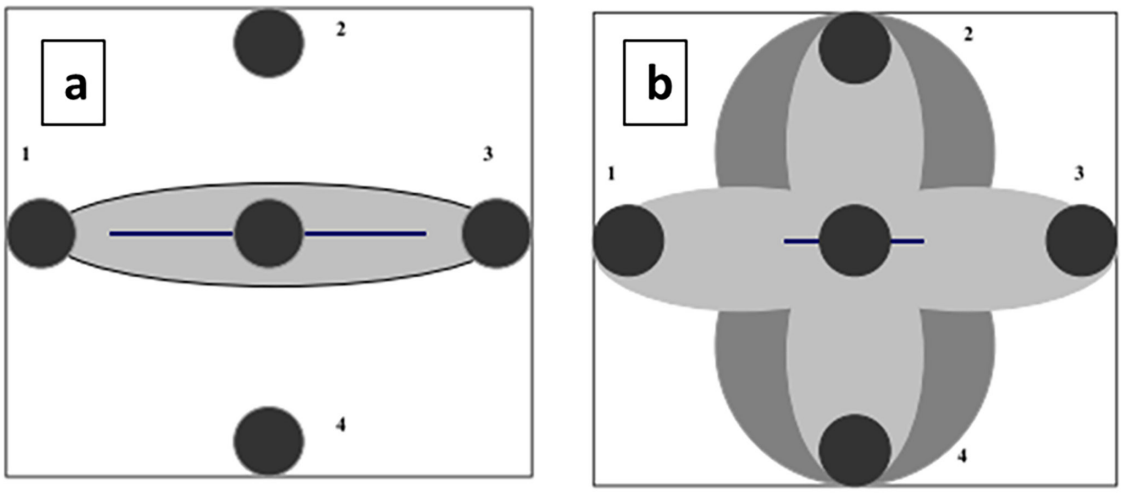

Fig. A-4—Five-spot pattern with a central injector and four producers showing fracture extension in the red line. (a) Weaker sweep efficiency with long fractures oriented to Producers 1 and 3. (b) Improvement in sweep for Producers 2 and 4 compared with 1 and 3. Adopted from Gadde and Sharma (2001).